Effects of Phospholipid Structure on the Acoustic Cavitation of Functionalized Mesoporous Silica Nanoparticles: Implications for Image-Guided Drug Delivery

Talaial B. Alina,[1] Hunter B. Kirkpatrick,[1] Natalie M. Bower, [1] Shane D. Curry, [1] Taylor R. Ausec,[1] Sven A. Saemundsson,[1] Evan N. Mueller,[1] C. Wyatt Shields IV,[1] Jennifer N. Cha,[1,] Andrew P. Goodwin[1,*]*

[1]Department of Chemical and Biological Engineering, University of Colorado Boulder, Boulder, Colorado 80303, United States

KEYWORDS: High-intensity focused ultrasound (HIFU), phospholipids, hydrophobicity, cavitation, mesoporous silica nanoparticles

This study investigates the acoustic response of phospholipid-coated, hydrophobically modified mesoporous silica nanoparticles (PL-HMSNs) for image-guided drug delivery. PL-HMSNs were first stabilized with a PEGylated lipid, DSPE-PEG2k-methoxy, and the effect of particle concentration on HIFU-induced cavitation threshold was explored. We found that increasing particle concentration from 0 to 200 μg/mL decreased the acoustic pressure threshold for cavitation

from ~14 to ~11 MPa, depending on the formulation. DPPC-, DSPC-, DOPC-, and DBPC-HMSNs gave similar cavitation thresholds. DLPC-stabilized particles showed little to no cavitation, which was attributed to DLPC's high critical micelle concentration. DOPC-HMSNs had higher uptake into HTB-9 human urinary bladder cancer cells than DSPC HMSNs, which is consistent with liposome delivery reports using unsaturated lipids. Finally, the effect of mixed lipid tail lengths was investigated by combining fluid-forming 1,2-dioleoyl-sn-glycero-3-phosphocholine (DOPC) with gel-forming lipids. Cavitation signal intensity for mixed lipids was significantly higher than that of pure lipids, which was ascribed to reduced line tension of mixed lipids. Our findings highlight that higher particle concentrations and longer lipid tail lengths can lower the cavitation threshold of PL-HMSNs, and combining saturated lipids with DOPC can amplify the cavitation response. These results provide insights for optimizing lipid-stabilized solid ultrasound contrast agents for drug delivery applications and show how common lipid formulations can be imparted with acoustic activity.

INTRODUCTION

Ultrasound, or acoustic waves with frequencies above human hearing range,[1] has primarily been used for imaging and diagnostic applications in both medicine and materials.[2] Higher ultrasound intensities can also facilitate inertial cavitation, or the formation of bubbles in solution. Once formed, these bubbles may undergo non-inertial oscillation and/or collapse into solution. Non-inertial, or stable, cavitation refers to the oscillation of a bubble about a central diameter,[3] typically at low ultrasound amplitudes, which can impart localized acoustic effects.[4,5] In one example, stable cavitation was used to promote the controlled opening of the blood-brain barrier in rat glioma models for the delivery of doxorubicin.[6] Stable cavitation of microbubbles has also been used to detect gastrointestinal bleeding.[7]

Higher intensity ultrasound may induce growth of the bubble by rectified diffusion and gradual dissolution of the bubble into solution.[8–10] This inertial collapse of bubbles into solution can release

a high amount of energy, which can temporarily increase surrounding temperatures up to 5000 K and pressures up to 250 MPa within the collapsing bubbles,[11] as well as produce high velocity jets that can damage surrounding structures.[12] Thus, deliberately-induced cavitation has been used to ablate tissues[13] and release drugs.[14] For example, Datta *et al.* applied ultrasound to lyse blood clots.[15] Similarly, Sackmann *et al.* employed shock-wave lithotripsy to break up gallbladder stones.[16] Stewart *et al.* used magnetic resonance-guided focused ultrasound surgery to treat uterine fibroids in women, [17] while Blana *et al.* applied high-intensity focused ultrasound (HIFU) for the localized treatment of prostate cancer.[18] However, nucleating cavitation requires high levels of energy that can create off-target effects like damaged healthy tissue.[19]

Contrast agents have been developed that can reduce the acoustic input intensities needed for cavitation, thereby limiting off-target effects. While in pure liquids, cavitation follows a high energy homogeneous bubble nucleation mechanism,[20] ultrasound contrast agents can instead stabilize gas nuclei that would otherwise dissolve into the bulk fluid. One such agent is a microbubble, which often contains perfluorocarbon gas stabilized in aqueous media by a combination of lipids, polymers, or albumin shells.[21] The responsiveness of microbubbles to ultrasound has been exploited for challenging applications like blood-brain barrier (BBB) disruption.[22] Other agents like phase-shift nanodroplets rely on ultrasound irradiation to vaporize superheated liquid nanodroplets to form gas bubbles. Guo *et al.* applied low-intensity pulsed ultrasound to nanodroplets consisting of perfluoropentane and vancomycin, and they observed a significant decrease in the activity of methicillin-resistant *S. aureus* biofilms compared to those without exposure to ultrasound.[23] The main disadvantage of microbubbles and nanodroplets is that they have limited lifetime in vivo, typically < 1 h.[24,25] Furthermore, microbubbles and nanodroplets

are often larger than 200 nm and thus cannot extravasate from the bloodstream.[26] As a result, these fluid-filled ultrasound contrast agents generally remain restricted to the vasculature.[19]

To address limitations in the size and stability of bubbles and droplets, solid contrast agents have also been developed. Rather than transporting a fluid into the body and expanding it, solid agents facilitate vaporization of ambient water by heterogeneous nucleation on the particle surface, and thus bubble nucleation is strongly dependent on the surface properties of the particle (Figure 1A). As the bubble is formed by the incident ultrasound pulse, and the employed ultrasound intensities employed are large, the most relevant mechanism is inertial rather than stable cavitation. However, such contrast agents can be used not only for therapeutic but imaging applications, as the readouts can be imaged on a conventional ultrasound scanner. Examples of these solid contrast agents include mesoporous silica nanoparticles (MSNs)[27,28] polymer nano- and microparticles (including nanocups with concave geometries),[29] and gold nanoparticles with roughened surfaces.[30] In previous work, the Goodwin group developed methods to produce ~100 nm sized phospholipid-coated, hydrophobically modified, mesoporous silica nanoparticles (PL-HMSNs). Hydrophobic modification prevented entry of water into the pores while the phospholipid capping layers dispersed the particles in water[31] and stabilized nascent bubbles on the surface. The lipid tail likely interacts with the octadecyltrichlorosilane functionalized on the silica surface.[32–34] The exclusion of water at these two hydrophobic surfaces drives the interactions between the 18-carbon chain of octadecyltrichlorosilane and the lipid tail, which enables them to associate.[34] As opposed to the limited lifetime of microbubbles, the PL-HMSNs retained acoustic activity for up to four months in phosphate-buffered saline.[35] PL-HMSNs facilitated cavitation at lower duty cycles (0.017%), spatial-average pulse-average intensities (I_{sapa}, 13 kW/cm^2), and spatial-average temporal-average intensities (I_{sata}, 1.3 W/cm^2), compared to values reported in the literature. Comparisons include

histotripsy, with an I_{sapa} between 22-44 kW/cm^2 and duty cycles between 0.2 and 9.1%,[36] and the vaporization of multifunctional microbubbles consisting of polymeric micelles and perfluoropentane, with an I_{sata} of 2 W/cm^2 and duty cycle of 20%.[37]

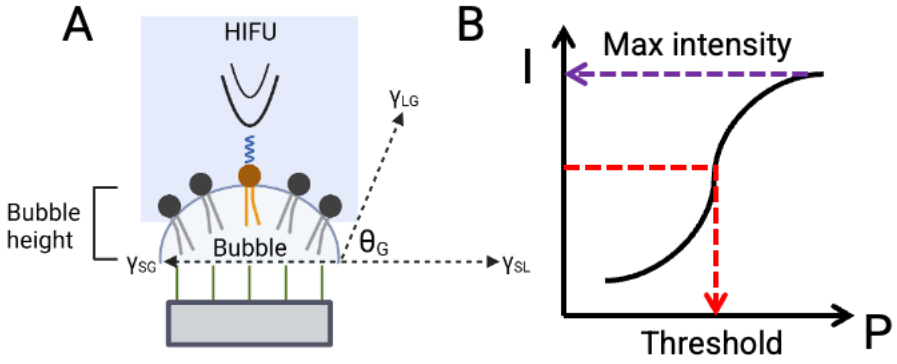

Figure 1. (A) Overview of cavitation bubble on PL-HMSN surface/water interface. For inertial cavitation to occur, the balance of interfacial tensions (ɣ) must favor bubble stability at a specific input pressure. The solid-gas (SG) interface relates to the hydrophobic modification of the HMSN, while the liquid-gas (LG) interface relates to the phospholipid monolayer. (B) Hypothetical output acoustic intensity vs. input pressure curve. The pressure at which 50% intensity is observed is the cavitation threshold, which relates to the interfacial energies of the cavitation bubble. The intensity at the top of the curve relates to the ultimate size of the bubble before collapse. SL: solid-liquid; θ_G: gas contact angle.

A potential advantage of PL-HMSNs is their phospholipid coating. More generally, as liposomes and lipid nanoparticles represent the dominant fraction of nanotechnologies approved in the clinic. Liposome composition can be modified for selective cell targeting and circulation time[38] by changing headgroup charge, lateral lipid phase, and phase separation.[39–42] Cancer cells

in particular rely on different pathways to acquire fatty acids necessary for growth,[43] and certain lipid types are overrepresented in certain tumor types. Colorectal[44] and breast[45] cancer cells preferentially uptake polyunsaturated fatty acids, which is a potential avenue for increasing the efficiency of drug delivery to tumors. The work detailed in this manuscript explores how the same lipids utilized for these applications can also be used to tune response to ultrasound stimulation.

Thus, while it would be desirable to combine the advantages of delivery by liposomes with acoustic responsiveness imparted by particles, it remains unclear how different lipid coatings could affect the ultrasound response of the PL-HMSNs. In PL-HMSNs, the role of lipid in cavitation is to stabilize the gas-liquid interface to allow bubble growth under ultrasound insonation (Figure 1A). The addition of lipids like 1,2-dioleoyl-sn-glycero-3-phosphocholine (DOPC, C18:1) could alter the fluidity of the lipid membrane, which might influence bubble nucleation. Addressing these gaps in knowledge could enable cavitation on PL-HMSNs at lower acoustic pressures and intensities, which is desirable for biomedical applications such as imaging and drug delivery.

Thus, the objective of this work was to investigate the cavitation responses of mesoporous silica nanoparticles (MSNs) and PL-HMSNs in water as a function of particle concentration and lipid composition. Cavitation response was quantified using two metrics. First, the input pressure at which half of maximum intensity occurs was defined as the cavitation threshold, which corresponds to ability of the interfacial components on the PL-HMSN to stabilize a cavitation bubble (Figure 1B). Second, the intensity of received signal at high pressure relates to the ultimate size of the bubble, which is related to the expansion modulus of the lipid monolayer. It was hypothesized that increased particle concentration could reduce the cavitation threshold because of cooperative interparticle interactions that contribute to bubble stabilization, thereby reducing

the energy needed to collapse a bubble.[46] It was also hypothesized that changing the composition of the lipid monolayer would change its expansion modulus, leading to changes in cavitation response, though not threshold. Mixing DOPC resulted in higher cavitation signal intensities for dipalmitoylphosphatidylcholine (DPPC, C16), distearoylphosphatidylcholine (DSPC, C18), and 1,2-dibehenoyl-sn-glycero-3-phosphocholine (DBPC, C22), with the effects more pronounced for DSPC and DBPC HMSNs. Lastly, in cell studies, the DOPC-coated HMSNs showed higher uptake into HTB-9 human bladder carcinoma cells than DSPC-coated HMSNs, showing the beneficial aspects of tuning lipid composition. Overall, these results show that higher particle concentrations, longer lipid tail lengths, and mixtures with DOPC were crucial for promoting cavitation on solid ultrasound contrast agents.

EXPERIMENTAL SECTION

Note: more detailed information on the Materials and Methods can be found in the Supporting Information.

Synthesis of phospholipid-coated, hydrophobically modified mesoporous silica nanoparticles (PL-HMSNs): Sub-100 nm sized MSNs were synthesized and were functionalized to make HMSNs following a previous report.[47] Phospholipid monolayers were deposited onto hydrophobically modified silica nanoparticles using a modified chloroform injection technique.[48] On the first day of the synthesis, stock solutions of 10 mg/mL lipids were dissolved in chloroform on the day of the experiment using powders previously stored at –20°C and equilibrated to room temperature when ready to use. Then, a stock solution of 5 mg/mL HMSNs were prepared in a 4 mL glass scintillation vial in chloroform and sonicated for 1 min for dissolution. Next, the lipid stock solutions were sonicated for 15 s.

Afterwards, 2.71 μmol lipid:0.0833 μmol DSPE-PEG2K-methoxy was combined with 3 mg HMSN from the stock solution in a 4 mL glass scintillation vial. In a separate 20 mL glass scintillation vial, 10 mM phosphate-buffer (PB) was stirred with a small rod-shaped stir bar at 1500 RPM for 10 min to equilibrate at the process temperature in an oil bath. The combined lipid-HMSN solution was sonicated for 15 s and then slowly injected into the PB solution while stirring at 1500 RPM, taking extra care when injecting into PB solution above the boiling point of chloroform (61.2°C). The 4 mL glass vials were washed with 300 μL chloroform to collect remaining particles; these vials were also sonicated for 15 s and their solutions were injected into the respective 20 mL vials. After the last injection, the combined lipid-HMSN-PB solution was mixed for 3 min at 1000 RPM, then stirred open overnight at the process temperature and 1500 RPM to evaporate the chloroform from the mixture.

The next day, the mixture was extracted into 1.5 mL microcentrifuge tubes and the reaction vessel was washed and sonicated for 15 s with 3 mL 10 mM PB to extract residual PL-HMSNs. Then, the solution was centrifuged at 10,000 relative centrifugal force (RCF) for 10 min to pellet the particles and remove excess lipids. The supernatant was centrifuged a second time separately at 10,000 RCF for 10 min to recover any remaining particles. The pellets remaining after the first and second centrifugations were combined into two separate solutions, respectively. Afterwards, the pellet from the first centrifugation was redispersed in 1 mL 10 mM PB and recentrifuged at 10,000 RCF for 10 min. Then, the supernatant was redispersed into the solution corresponding to the second centrifugation and centrifuged at 10,000 RCF for 10 min. The pellets from the two centrifugations were combined and then redispersed in 1 mL 10 mM PB. Samples were prepared by dilution with ultrapure water.

HIFU setup: The HIFU setup was adopted from previous work.[47,49–54] Prior to the experiment, the water bath was thoroughly cleaned with soap and deionized water. Then, the water bath was filled up to a 4.5" height with deionized water. Next, a coupling cone (Sonic Concepts C101), housing a 1.1 MHz transducer (Sonic Concepts H-101, 64.0 mm active diameter by 63.2 mm radius of curvature), was placed in the deionized water bath that filled the cone with water. Then, a waveform generator (Agilent Technologies, 33522A) was connected to an amplifier (T&C Power Conversion AG1020 amplifier). The parameters on the waveform generator were: burst period: on and 100 ms (10 Hz), channel: 1, frequency: 1.1 MHz, number of cycles: 12 (duty cycle: 0.011%), waveform: sine wave. The signal from the waveform generator was sent to the amplifier, which was operating at 100% amplification and 55 ± 1.5 dB gain. The amplifier then sent the amplified signal to an impedance-matching network (Sonic Concepts, S/N 119) that was then connected to the 1.1 MHz transducer, housed in a coupling cone, filled earlier with deionized water from the water bath, and placed 6 cm away from the sample holder (2 mL of sample in a 3 mL Falcon pipette bulb). The focal volume, according to the manufacturer, was about 15 μL (1.37 mm diameter by 10.21 mm focal length). The transducer converted the electrical signal into sound energy directed onto the pipette bulb. A 20 MHz transducer (Olympus Parametrics V317), orthogonal to the 1.1 MHz transducer and touching the sample holder, was then used to record and convert the resultant pressure wave of the bubble collapse into electrical signals. These signals were then amplified with a gain of 40 dB using a pulser/receiver (Olympus 5072PR) with the pulse repetition frequency set at 100, energy at 1, damping at 3 (50 ohms). The amplified signal was then filtered with a 6.7 MHz high pass filter (Thorlabs EF513) and outputted to an oscilloscope (Tektronix TBS1000). The oscilloscope averaged the data every 16 data points and was set with a y-axis interval of 200 mV and an x-axis interval of 25 μs. Input voltages into the waveform

generator were varied from 0–1000 mVpp (millivolt-peak-to-peak) and samples were typically treated with HIFU insonation for 30 s.

Statistical testing: Statistical analysis was conducted in GraphPad 9.5.1. Data were first tested for normality using a QQ plot. Agonist vs. response with variable slope and four parameters was fitted onto the intensity profiles. The EC50 metric containing a 95% confidence interval from these profiles was used to define the cavitation threshold, which was assumed to be the acoustic pressure at half the maximum signal intensity. A two-way ANOVA with a post-hoc Tukey test was used to compare the effects of different ratios of DOPC (C18:1):D?PC (where ? = P, S, or B) on the signal intensity of coated PL-HMSNs. A p value of 0.01 was the minimum value required to reject the null hypothesis.

RESULTS AND DISCUSSION

The PL-HMSNs used in this study were prepared by conjugating an alkyl silane to the MSN surface, then reformulating in different phospholipids (Figure 2A-B, Table S1).[48,49] Briefly, ~100 nm sized MSNs were first prepared and then functionalized with octadecyltrichlorosilane.[47] The hydrophobic MSNs were then suspended with DLPC, DPPC, DSPC, DOPC, or DBPC, along with 3.0 mol% DSPE-PEG2K-methoxy for stability, to form PL-HMSNs. TEM images confirmed that the MSNs, HMSNs, and PL-HMSNs were all spherical with diameters of less than 100 nm (Figure 2C). Furthermore, dynamic light scattering (DLS) measurements revealed MSNs to have a peak diameter of 130 ± 40 nm and HMSNs had two peaks consisting of 370 ± 44 nm and 2100 ± 320 nm, respectively, indicating that some aggregation was present (Figure S1). The hydrophilicity and hydrophobicity of the MSNs, HMSNs, and PL-HMSNs were then validated through contact angle measurements of particles deposited on a glass surface. A clean glass slide (39.5 ± 1.2°) and

surfactant-extracted MSN samples had much lower contact angles (18.3 ± 1.3°) than the hydrophobically modified HMSN samples (132.3 ± 0.5°). The addition of phospholipids decreased the contact angle of HMSN samples; for example, this effect was demonstrated in the contact angle of DPPC HMSNs (68.7 ± 1.5º) (Figure 2D). While we acknowledge that static contact angle is an imperfect method of measuring hydrophobicity or hydrophilicity of a particle film, the large changes in these values at each point in the synthesis provide confidence that the functionalization worked as intended.[55,56] Phospholipid association with silica nanoparticles was determined by analysis of ^{1}H NMR spectra. For this measurement, ^{1}H NMR spectra of pure DLPC, DPPC, DSPC, DOPC, DBPC, and DSPE-PEG2K-methoxy were first taken in deuterated chloroform. Then, 3 mg/mL PL-HMSNs containing different compositions of these lipids were dispersed in 1 mL deuterated chloroform. ^{1}H NMR spectroscopy revealed that PL-HMSNs with DOPC, containing mixed lipid compositions, fell within 10% of the lipid molar ratio added (Figure S2, Table S2).

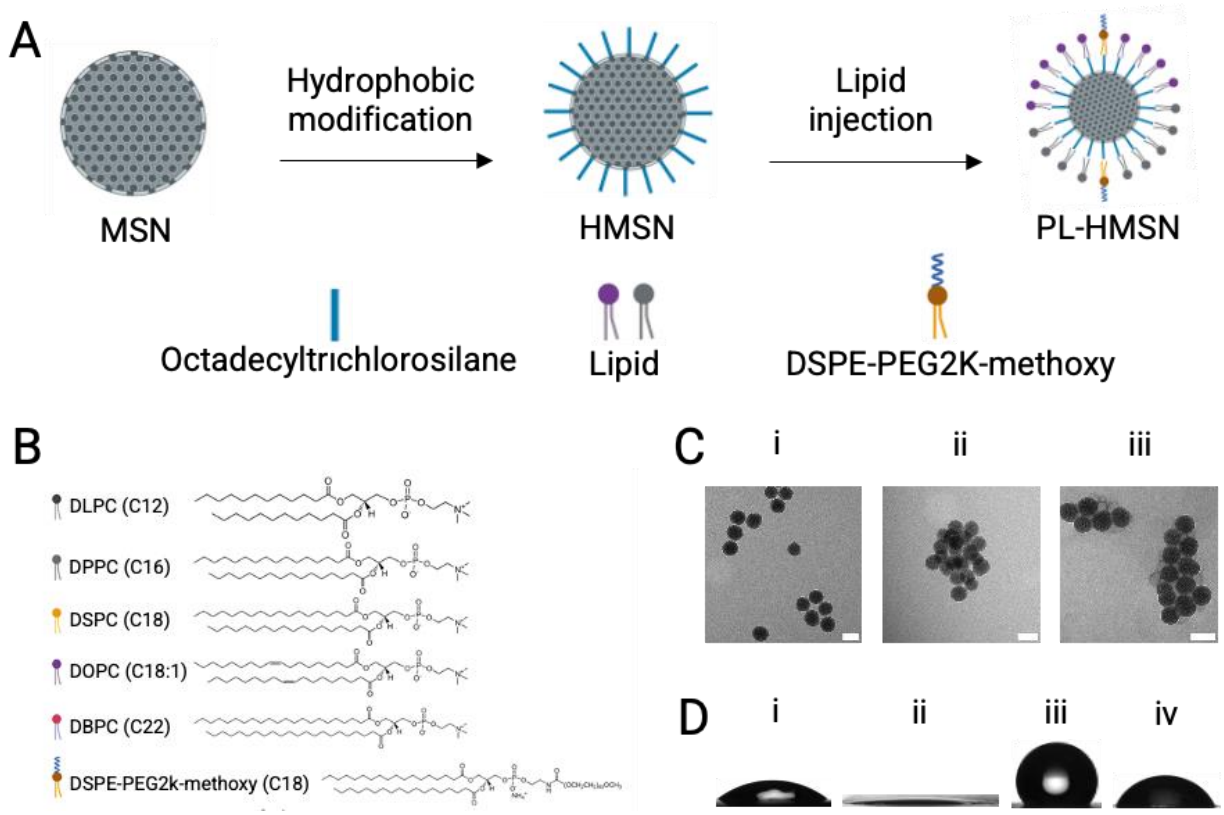

Figure 2. (A) Synthesis of phospholipid-coated, hydrophobically modified mesoporous silica nanoparticles (schematic not to scale). MSN: mesoporous silica nanoparticle; HMSN: hydrophobically modified mesoporous silica nanoparticle; PL-HMSN: phospholipid-coated, hydrophobically modified mesoporous silica nanoparticle. (B) Chemical structures of lipids investigated. (C) TEM images of (i) MSNs, (ii) HMSNs, and (iii) DPPC HMSNs. Scale bar = 100 nm. (D) Contact angle measurements of (i) a blank glass slide (39.5 ± 1.2°), (ii) MSNs (18.3 ± 1.3°), (iii) ODTS-modified MSNs (132.3 ± 0.5°), and (iv) DPPC PL-HMSNs (68.7 ± 1.5°). Images cropped to remove water dropper.

After confirming the hydrophobicity and lipid functionalization of the PL-HMSNs, they were tested for cavitation under acoustic stimulation (Figure S3). Ultrasound insonation conditions were held at 1.1 MHz frequency, 10 Hz repetition rate, and 30 s total treatment time, while peak negative

pressure was varied from 0 to 14.31 MPa (Figure S4, Figure S5, Table S3). The proportional volume of sample exposed to ultrasound is equivalent to 15 μL based on reported specifications for the focal diameter and focal length of the Sonic Concepts H-101 transducer. From the relative intensity calculations and dose-response plots (Figure S6), the highest intensity was recorded. The input pressure at half of the maximum intensity was also extracted and defined as the cavitation threshold.[49,57]

First, the concentrations of DLPC, DPPC, DSPC, DOPC, and DBPC HMSNs were varied from 0 to 200 μg/mL, followed by testing their acoustic responses to HIFU. Ultrapure water (UP), 0 μg/mL PL-HMSN, and 200 μg/mL MSN samples were tested as negative controls. When investigating the thresholds within these intensity profiles, suspensions with higher particle concentrations could be cavitated at lower thresholds (Figure 3), where increasing the particle concentration from 25 to 200 μg/mL reduced the cavitation threshold by about 1 MPa. A one-tailed Spearman correlation analysis (used in anticipation of non-normality) found a significant negative correlation between particle concentration and cavitation threshold, excluding particles with DLPC (*$p < 0.05$, **$p < 0.02$, Table S4). At common concentrations, the thresholds were mostly comparable for lipids with 16 and 22 carbon tail lengths. One possible reason for the comparable cavitation thresholds for the C16–C22 lipids is that C18 and C22 lipids have comparable area expansion moduli,[58] so similar amounts of energy are used to expand a bubble nucleus. An exception to both trends was found with DLPC HMSNs, which did not show cavitation in the concentration range of 0–100 μg/mL at 14.31 MPa, the highest pressure tested, which aligns with a past report.[59] Some cavitation was observed at 200 μg/mL, although the signal was small and comparable to MSNs and UP controls (Figure 3). As ultrapure water was unable to undergo cavitation, pre-focal cavitation was excluded as a contributing factor. As a conservative

estimate for liposomes carried through to HIFU testing, 200 µg/mL DPPC liposomes were prepared based off the lipid concentrations found in the particle pellet (Table S5, and see Supporting Information for how this number was estimated), and these liposomes had comparable HIFU intensity profiles to ultrapure water and MSN controls, with signal intensity near 0 (Figure S7).

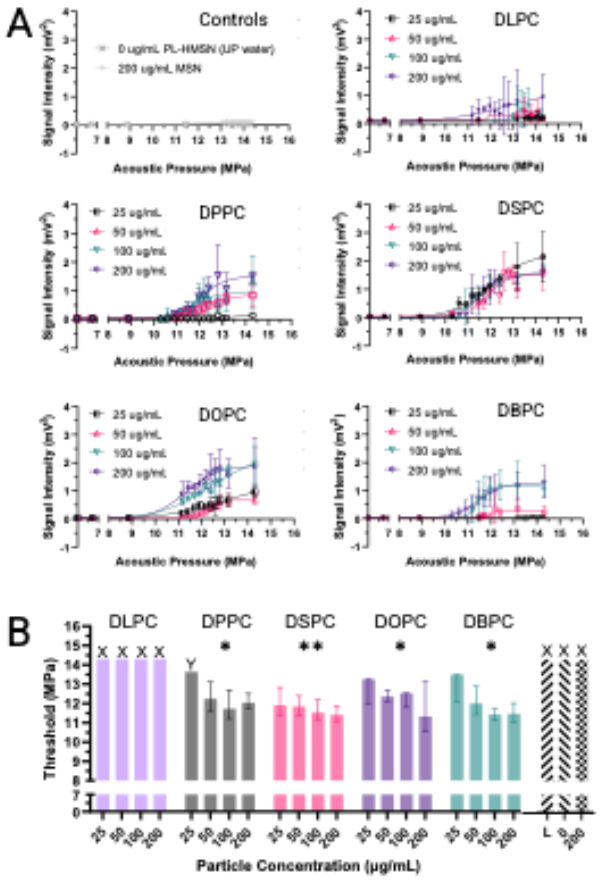

Figure 3. (A) Acoustic activity generated from pressure sweeps of 0 µg/mL PL-HMSNs (UP water), and 200 µg/mL MSNs and different concentrations of PL-HMSNs coated with DLPC (C12), DPPC (C16), DSPC (C18), DOPC (C18:1), and DBPC (C22). Intensity profiles represent acoustic emissions generated at 30 s treatment time (n = 3). Error bars signify one standard

deviation of mean. (B) Comparison of cavitation thresholds between different particle concentrations. At right, 0 denotes ultrapure water, and 200 denotes 200 μg/mL MSNs or DPPC liposomes. X denotes that no cavitation was detected in the pressure range tested. Y denotes that the confidence intervals were unable to be calculated. n = 3 replicates per data. Error bars signify 95% confidence interval.

The intensity profiles of the different PL-HMSNs were also examined. Different concentrations of DLPC HMSNs did not influence the acoustic output except for 200 μg/mL, for which signal intensity was still near 0 (Figure 3). As particle concentration increased for DPPC and DBPC HMSNs, the signal intensity increased. DSPC and DOPC HMSNs had intensity profiles within error at various concentrations. Also, while it was hypothesized that increasing particle concentration would increase particle aggregation, resulting in a higher number of nucleation sites available for cavitation, no correlation was found between threshold and hydrodynamic diameter (Figure S8).

The observation that increasing particle concentration reduces cavitation threshold is supported by several literature reports of other systems.[60–64] For example, Deng et al. applied an insonation frequency of 2.5 MHz, a pulse repetition frequency of 1 kHz, and a pulse duration of 8.3 μs to 100 nm hydrophobic polystyrene spheres. They found that increasing their concentration from 6.2×10^6 to 6.2×10^9 particles mL^{-1} decreased the cavitation threshold from 2.48 ± 0.35 MPa to 1.56 ± 0.26 MPa.[62] In another study, Gu et al. found that increasing the concentration of 20 nm hydrophilic silica nanoparticles from 0.15 to 1.5% (v/v) modestly reduced their cavitation threshold from approximately 28 to 27 MPa under the insonation of a 1 MHz transducer.[60] Using a 1.1 MHz transducer, Chen et al. found that increasing the concentration of 23 μm hydrophilic

silica microparticles from 0.2 g/L to 1 g/L decreased their cavitation threshold from 1.36 to 0.86 MPa.[65] Here, we theorize that increasing particle concentration allows more cooperative effects for stabilizing growing bubbles.

These results were compared to the phase behavior of lipids on the particle surface, which was probed using Laurdan dye. It was originally theorized in a previous report that liquid phase lipids would quench cavities available for the cavitation of bubbles.[59] DPPC, DSPC, and DBPC on HMSNs had comparable generalized polarization values ranging from 0.5 to 0.6, which indicated the presence of a highly gel-like membrane (Figure S9A-B), whereas both pure DOPC and pure DLPC on HMSNs exist as liquid phases at room conditions due to their low transition temperatures. Yet, DOPC had a measurable cavitation threshold of 11.33 MPa at 200 μg/mL, whereas cavitation with DLPC HMSNs was hard to detect (Figure 3). Thus, a more likely explanation is that cavitation threshold depends on hydrophobicity rather than the lipid phase.

Hydrophobicity is important because the inception of a cavitation bubble depends on the balance of surface and interfacial tensions at the air-gas-water contact line. If lipid monolayer coverage is poor, the bubble cannot be stabilized, and cavitation does not proceed. DOPC,[66] DPPC,[67] DSPC,[68] and DBPC are all hydrophobic with vanishingly small solubilities in water. In contrast, DLPC's water solubility is much larger (4 ppm, or ~0.22 mM) than any of the other lipids tested.[67] It is possible then that there are gaps in the DLPC monolayer that render the particle unable to stabilize a nascent cavitation bubble (Figure 1A). At higher particle and corresponding lipid concentrations, there is additional lipid in solution to fill these gaps.

These studies motivated an investigation into the effect of unsaturated and saturated lipid coated HMSNs on the loading of DiO as a model drug. DiO is a green fluorescent, lipophilic dye that can incorporate into lipid matrices.[69] Previous work in our group showed that DiO could be loaded

onto DPPC covered, silica coated gold nanorods.[70] Here, the encapsulation efficiency (mass of DiO per mass of DiO fed) of DiO in DOPC HMSNs was 4.0 ± 0.8 % in which was significantly lower than that of DSPC HMSNs: 15.1 ± 3.6 % (*$p < 0.05$) (Figure S10). The loading capacity (mass of DiO per mass of particle) of DiO in DOPC HMSNs was 0.8 ± 0.2 %, which was significantly lower than that of DSPC HMSNs: 3.0 ± 0.7 % (*$p < 0.05$). MSNs could not load DiO because of their lack of hydrophobicity, aligning with a past report.[70]

Because the advantage of PL-HMSNs over liposomes is their ability to sensitize cavitation, the next step was to determine how effectively PL-HMSNs could deliver drugs to cells. Since DiO loading could be quantified in HMSNs, DiO was chosen as the fluorescent lipid tag to image the uptake of the lipid coated HMSNs into cells. To investigate this hypothesis, HTB-9 human bladder cancer cells were incubated with either DOPC- or DSPC-HMSNs for 24 h to allow particle uptake. In fluorescence microscopy images of these cells (Figure 4A-C), the green fluorescence from the DiO-labeled particle shows strong correlation with the blue HTB-9 nuclei (Hoechst).

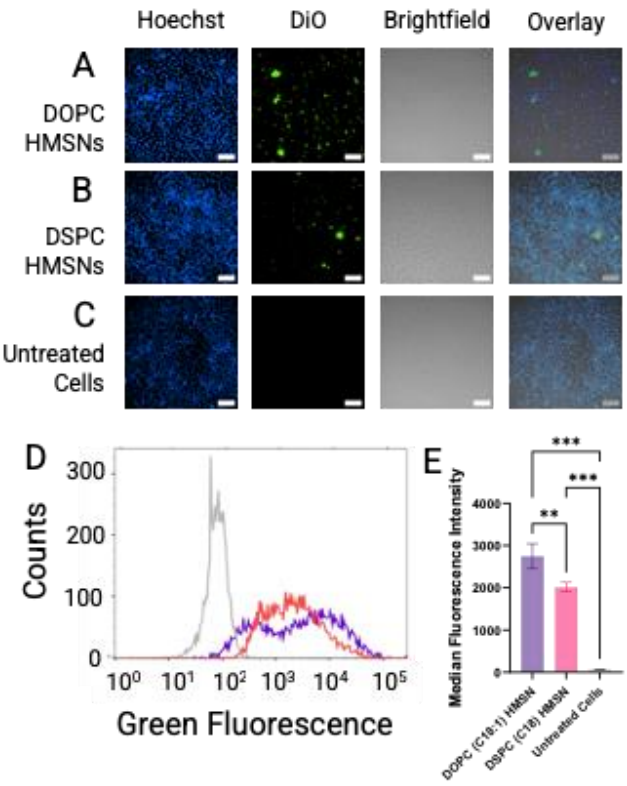

Figure 4. (A) Representative images of (A) DOPC-HMSNs and (B) DSPC-HMSNs uptaken into HTB-9 cells. (C) Representative image HTB-9 cells without particles. Scale bars = 100 µm. (D) Representative flow cytometry histograms of DOPC-HMSNs (purple) DSPC-HMSNs (red), and cells with no particles (gray). (E) n = 3 replicates for all data in this figure. Error bars signify one standard deviation of mean. Statistical significance was found using a one-way ANOVA and Tukey's HSD (**$p < 0.01$, ***$p < 0.001$).

To quantify particle uptake, cells were detached, and their fluorescence was recorded by flow cytometry. Notably, cells containing DOPC HMSNs had significantly higher median cell fluorescence than cells with DSPC HMSNs (**$p < 0.01$) while cells with lipid coated HMSNs had significantly higher median cell fluorescence than cells without particles (***$p < 0.001$) (Figure 4D-E), where similar bimodal distributions have been observed in similar analyses of cell uptake

of drug carriers.[71] These findings were surprising because DSPC-HMSNs showed higher loadings of DiO than DOPC-HMSNs did (Figure S10).

It was hypothesized that HMSNs coated with unsaturated lipids, like DOPC, would have enhanced uptake into cells compared to saturated lipids like DSPC. Such results are supported by previous studies. For example, Abumanhal-Masarweh *et al*. found higher uptake of DOPC (18:1) than HSPC (18:0) in 4T1 mouse breast carcinoma.[45] They reasoned that 4T1 cells have a high level of monounsaturated lipids and may preferentially uptake unsaturated lipids. Furthermore, Ho *et al*. found that mouse bladder carcinoma cells (MB49) had a higher number of unsaturated lipids than healthy bladder cells, and then used a complex of alpha-lactalbumin and oleic acid as a tumoricidal agent.[72] Furthermore, cancer cells are thought to uptake DOPC because they can use exogenous lipids for the provision of unsaturated fatty acids needed for growth.[73] This hypothesis is supported by the prevalence of unsaturated fatty acids in both colorectal[43] and breast[45] cancers, as cancer cells rely on different pathways to acquire fatty acids necessary for growth.[43] Thus, these results encourage further exploration of how coating HMSNs with different lipid compositions affects cell uptake.

However, a typical liposome formulation is not just DOPC. Because it has multiple components, often including saturated or unsaturated lipids, lipid-polymer conjugates, and cholesterol, so the effect of mixed lipid monolayers on cavitation intensity was investigated next. Interestingly, mixing DOPC with saturated lipids changed the intensity of the received signal but not the cavitation threshold (Figure 5A, Figure S11). First, no relationship was found between the cavitation threshold and molar ratio of DOPC:gel phase lipid HMSNs (Figure 5A), and there was also no relationship between the length of the lipid tail and the cavitation threshold (Figure 5A). However, mixing DLPC with DSPC suppressed cavitation for HMSNs completely (Figure S12).

Thus, even the presence of DLPC domains likely destabilized the initiation of cavitation. Furthermore, as before, no relationship was established between the threshold and the hydrodynamic diameter of the particles (Figure S13). Thus, the mixing of two cavitation-stabilizing lipids did not seem to affect cavitation inception, which is consistent with data showing similar cavitation inception for different lipid coatings.

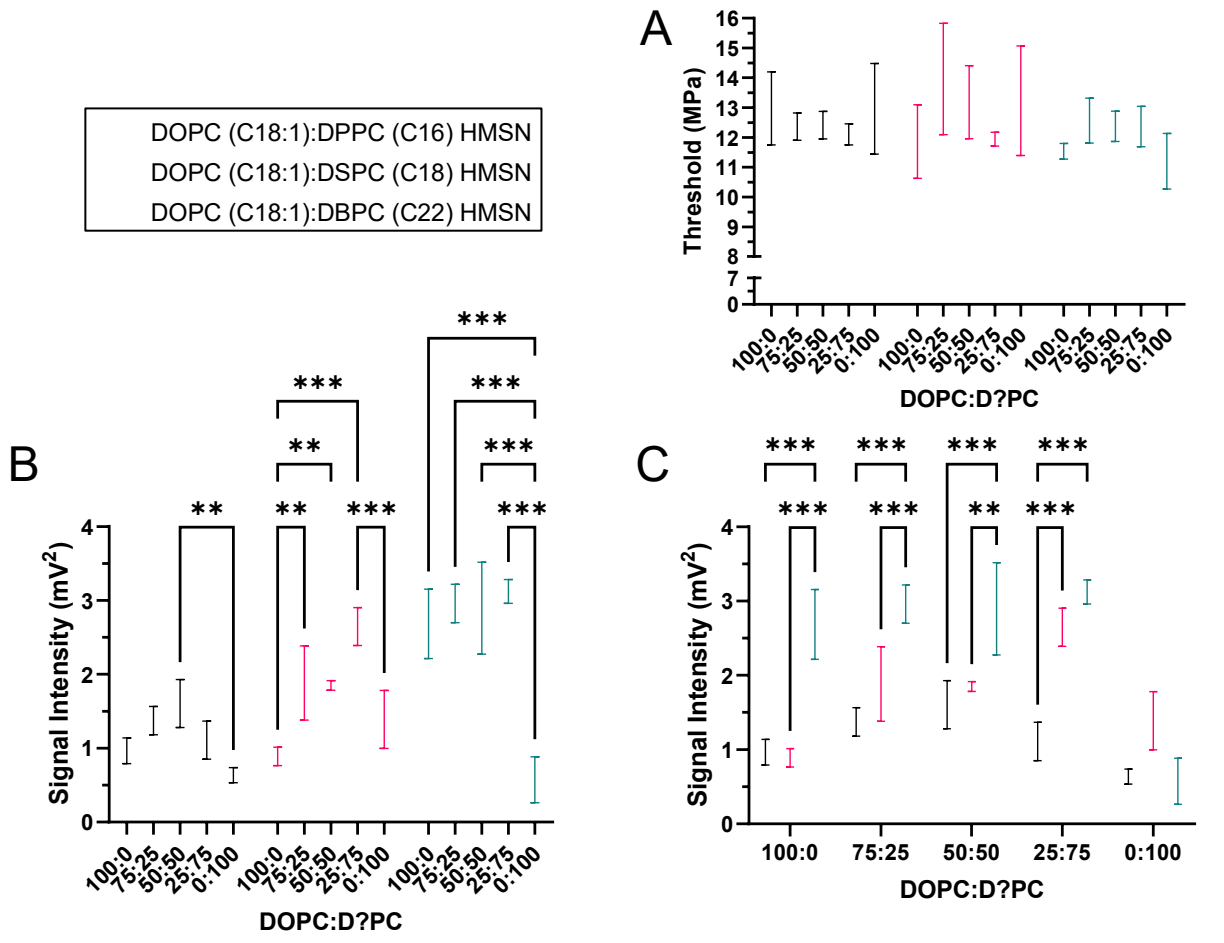

Figure 5. (A) Comparison of thresholds between different lipid molar ratios for each 200 µg/mL DOPC:D?PC PL-HMSN mixture. Error bars signify 95% confidence interval for pressure at half the maximum intensity. (B) Comparison of signal intensities between different DOPC:D?PC HMSN mixtures for each lipid molar ratio at 14.31 MPa (**$p < 0.01$, ***$p < 0.001$). Error bars

signify one standard deviation of mean. (C) Comparison of signal intensities between different lipid molar ratios for each DOPC:D?PC mixture at 14.31 MPa (**$p < 0.01$, ***$p < 0.001$). Error bars signify one standard deviation of mean. n = 3 replicates for all data in this figure. Statistical significance for 4B and 4C was tested using a two-way ANOVA with Tukey's post-hoc test.

However, lipid mixtures showed consistently higher output acoustic intensities than single component lipids did (Figure 5B-C, S10). This finding is consistent with other reports that mixed lipid monolayers exhibit reduced line tension owing to the formation of domains,[74,75] which in turn allows a mixed lipid monolayer to be deformed more easily than a pure lipid monolayer, and thus the cavitation bubble can reach a larger ultimate size (Figure 1). Indeed, Laurdan probe studies[76] (Figure S9) showed that mixtures of 25:75, 50:50, and 75:25 DOPC:DPPC, DOPC:DSPC, and DOPC:DBPC contain coexisting fluid and gel phases or domains, which was supported by literature reports.[77–79] Differences in signal intensity were also found across different lipid mixtures with the same relative compositions. 75:25, 50:50, and 25:75 DOPC:DBPC all showed significantly higher signal intensities than the matching compositions with DOPC:DPPC- and DOPC:DSPC-HMSNs (***$p < 0.001$) (Figure 5C). However, because 100:0 DOPC:DBPC-HMSNs had significantly higher signal intensities than 0:100 DOPC:DBPC-HMSNs, there appears to be no effect of DBPC addition to the system. A possible reason for this observation is that the mutual solubility of DOPC and DBPC is likely low, so domain sizes are fixed already upon DBPC addition. Although 0:100 DOPC:DSPC-HMSNs had higher signal intensities than 0:100 DOPC:DPPC- and 0:100 DOPC:DBPC-HMSNs, these differences were not statistically significant. It is possible that comparable gel-like membrane states show a similar intensity of cavitation response (Figure 5B). Interestingly, 100:0 DOPC:DBPC-HMSNs had significantly

higher signal intensities than 100:0 DOPC:DPPC- and DOPC:DSPC-HMSNs, likely caused by the increased preparation temperature when working with high-melting DBPC (***$p < 0.001$). This observation motivates a future investigation of preparation temperature on the echogenicity of solid ultrasound contrast agents. Taken together, these conclusions support the claim that mixing lipids on HMSN monolayers increases the cavitation intensity without changing inception, likely due to reduced line tension caused by domain formation. Thus, the addition of DOPC appears to increase acoustic cavitation intensity not directly due to its unsaturated character but due to the ability of unsaturated lipids to phase separate from saturated lipids.

CONCLUSION

It is important for solid ultrasound contrast agents to promote strong cavitation events at low acoustic energy inputs to minimize off-target effects. Here, it is reported that increased PL-HMSN concentration and long lipid tail lengths were crucial for reducing cavitation thresholds from beyond system limits of 14.31 MPa to approximately 11 MPa. Additionally, DOPC had significantly higher uptake into HTB-9 human urinary bladder cancer cells. While the addition of DOPC to gel phase lipids on HMSNs did not substantially affect cavitation thresholds, it did result in an enhanced signal intensity, and therefore acoustic response. Future research should investigate how changing lipid composition affects cell viability. Other areas include investigating how modifying the surface chemistry of PL-HMSNs affects their transport through relevant biological fluids like mucus. Finally, future directions include studying the effect of different lipid surface chemistries on site-directed release of cargo to optimize PL-HMSN facilitated treatment of tumors.

ASSOCIATED CONTENT

Supporting Information.

Detailed experimental procedures, detailed analysis procedures, Dynamic Light Scattering plots, NMR spectra, HIFU calibration information, output signal intensity vs. input pressure curves, plots of cavitation threshold vs. hydrodynamic diameter, Laurdan emission spectra, DiO encapsulation and loading plots, 18:1 Lissamine Rhodamine B and Naphthopyrene encapsulation and loading plots.

AUTHOR INFORMATION

Corresponding Author

*jennifer.cha@colorado.edu, *andrew.goodwin@colorado.edu

Author Contributions

The manuscript was written through contributions of all authors. All authors have given approval to the final version of the manuscript.

Funding Sources

NSF CBET 2025547, NIH R21CA267608, DoEd P200A210114

ACKNOWLEDGMENT

This work was supported by NSF CBET 2025547 and NIH R21CA267608, and T.B.A., T.R.A., and E.N.M. were partially supported by a Graduate Assistance in Areas of National Need (GAANN) grant, P200A210114. The authors thank the Electron Microscopy Service at CU Boulder for the use of their FEI Tecnai T12 Spirit, 120 kV LaB6 filament TEM. The authors also thank the BioFrontiers Nuclear Magnetic Resonance Facility for the use of their 400MHz Bruker

NMR, as well as Prof. Theodore Randolph for the use of his Anton Paar Litesizer. Drs. Thomas Flaig and Lih-Jen Su kindly provided HTB-9 cells. The authors also thank the Flow Cytometry Shared Facility in the Jennie Smoly Caruthers Biotech Building funded by NIH grant S10ODO21601. Illustrations were created with BioRender.com. ChemDraw 21.0.0 was used to generate publication quality images of molecules downloaded from Avanti Polar Lipids. GraphPad Prism 9.5.1 was used to generate S-curve plots for cavitation threshold determination and perform statistical analyses.

REFERENCES

(1) Tomás-Pejó, E.; Alvira, P.; Ballesteros, M.; Negro, M. J. Pretreatment Technologies for Lignocellulose-to-Bioethanol Conversion. In *Biofuels*; Elsevier, 2011; pp 149–176.
(2) Ter Haar, G. Therapeutic Applications of Ultrasound. *Progress in biophysics and molecular biology* **2007**, *93* (1–3), 111–129.
(3) Coussios, C. C.; Roy, R. A. Applications of Acoustics and Cavitation to Noninvasive Therapy and Drug Delivery. *Annu. Rev. Fluid Mech.* **2008**, *40*, 395–420.
(4) Prosperetti, A. Bubble Phenomena in Sould Fields: Part Two. *Ultrasonics* **1984**, *22* (3), 115–124. https://doi.org/10.1016/0041-624X(84)90006-4.
(5) Prosperetti, A. Thermal Effects and Damping Mechanisms in the Forced Radial Oscillations of Gas Bubbles in Liquids. *The Journal of the Acoustical Society of America* **1977**, *61* (1), 17–27. https://doi.org/10.1121/1.381252.
(6) Sun, T.; Zhang, Y.; Power, C.; Alexander, P. M.; Sutton, J. T.; Aryal, M.; Vykhodtseva, N.; Miller, E. L.; McDannold, N. J. Closed-Loop Control of Targeted Ultrasound Drug Delivery across the Blood–Brain/Tumor Barriers in a Rat Glioma Model. *Proceedings of the National Academy of Sciences* **2017**, *114* (48), E10281–E10290. https://doi.org/10.1073/pnas.1713328114.
(7) Vaezy, S.; Luo, W.; Bailey, M.; Crum, L.; Rabkin, B.; Zderic, V. Stable Cavitation in Ultrasound Image-guided High Intensity Focused Ultrasound Therapy. *The Journal of the Acoustical Society of America* **2007**, *122* (5), 3077–3078. https://doi.org/10.1121/1.2942992.
(8) Church, C. C. Prediction of Rectified Diffusion during Nonlinear Bubble Pulsations at Biomedical Frequencies. *J Acoust Soc Am* **1988**, *83* (6), 2210–2217. https://doi.org/10.1121/1.396349.
(9) Zhang, Y.; Li, S. A General Approach for Rectified Mass Diffusion of Gas Bubbles in Liquids Under Acoustic Excitation. *Journal of Heat Transfer* **2014**, *136* (4). https://doi.org/10.1115/1.4026089.
(10) Holt, R.; Roy, R. Bubble Dynamics in Therapeutic Ultrasound; Doinikov, A., Ed.; Research Signpost, 2005.

(11) Merouani, S.; Hamdaoui, O.; Rezgui, Y.; Guemini, M. Theoretical Estimation of the Temperature and Pressure within Collapsing Acoustical Bubbles. *Ultrason Sonochem* **2014**, *21* (1), 53–59. https://doi.org/10.1016/j.ultsonch.2013.05.008.
(12) Miller, M. W.; Miller, D. L.; Brayman, A. A. A Review of in Vitro Bioeffects of Inertial Ultrasonic Cavitation from a Mechanistic Perspective. *Ultrasound in medicine & biology* **1996**, *22* (9), 1131–1154.
(13) Orsi, F.; Zhang, L.; Arnone, P.; Orgera, G.; Bonomo, G.; Vigna, P. D.; Monfardini, L.; Zhou, K.; Chen, W.; Wang, Z. High-Intensity Focused Ultrasound Ablation: Effective and Safe Therapy for Solid Tumors in Difficult Locations. *American journal of roentgenology* **2010**, *195* (3), W245–W252.
(14) Pitt, W. G.; Husseini, G. A.; Staples, B. J. Ultrasonic Drug Delivery–a General Review. *Expert opinion on drug delivery* **2004**, *1* (1), 37–56.
(15) Datta, S.; Coussios, C.-C.; Ammi, A. Y.; Mast, T. D.; de Courten-Myers, G. M.; Holland, C. K. Ultrasound-Enhanced Thrombolysis Using Definity® as a Cavitation Nucleation Agent. *Ultrasound in medicine & biology* **2008**, *34* (9), 1421–1433.
(16) Sackmann, M.; Delius, M.; Sauerbruch, T.; Holl, J.; Weber, W.; Ippisch, E.; Hagelauer, U.; Wess, O.; Hepp, W.; Brendel, W.; Paumgartner, G. Shock-Wave Lithotripsy of Gallbladder Stones. *New England Journal of Medicine* **1988**, *318* (7), 393–397. https://doi.org/10.1056/NEJM198802183180701.
(17) Stewart, E. A.; Rabinovici, J.; Tempany, C. M. C.; Inbar, Y.; Regan, L.; Gastout, B.; Hesley, G.; Kim, H. S.; Hengst, S.; Gedroye, W. M. Clinical Outcomes of Focused Ultrasound Surgery for the Treatment of Uterine Fibroids. *Fertility and Sterility* **2006**, *85* (1), 22–29. https://doi.org/10.1016/j.fertnstert.2005.04.072.
(18) Blana, A.; Walter, B.; Rogenhofer, S.; Wieland, W. F. High-Intensity Focused Ultrasound for the Treatment of Localized Prostate Cancer: 5-Year Experience. *Urology* **2004**, *63* (2), 297–300. https://doi.org/10.1016/j.urology.2003.09.020.
(19) Thomas, R. G.; Jonnalagadda, U. S.; Kwan, J. J. Biomedical Applications for Gas-Stabilizing Solid Cavitation Agents. *Langmuir* **2019**, *35* (31), 10106–10115. https://doi.org/10.1021/acs.langmuir.9b00795.
(20) Briggs, H. B.; Johnson, J. B.; Mason, W. P. Properties of Liquids at High Sound Pressure. *The Journal of the Acoustical Society of America* **1947**, *19* (4), 664–677.
(21) Correas, J.-M.; Bridal, L.; Lesavre, A.; Méjean, A.; Claudon, M.; Hélénon, O. Ultrasound Contrast Agents: Properties, Principles of Action, Tolerance, and Artifacts. *European radiology* **2001**, *11* (8), 1316–1328.
(22) McDannold, N.; Arvanitis, C. D.; Vykhodtseva, N.; Livingstone, M. S. Temporary Disruption of the Blood–Brain Barrier by Use of Ultrasound and Microbubbles: Safety and Efficacy Evaluation in Rhesus Macaques. *Cancer Research* **2012**, *72* (14), 3652–3663. https://doi.org/10.1158/0008-5472.CAN-12-0128.
(23) Guo, H.; Wang, Z.; Du, Q.; Li, P.; Wang, Z.; Wang, A. Stimulated Phase-Shift Acoustic Nanodroplets Enhance Vancomycin Efficacy against Methicillin-Resistant Staphylococcus Aureus Biofilms. *Int J Nanomedicine* **2017**, *12*, 4679–4690. https://doi.org/10.2147/IJN.S134525.
(24) Goertz, D. E.; Wright, C.; Hynynen, K. Contrast Agent Kinetics in the Rabbit Brain during Exposure to Therapeutic Ultrasound. *Ultrasound in medicine & biology* **2010**, *36* (6), 916–924.

(25) Kawabata, K.; Asami, R.; Azuma, T.; Umemura, S. Acoustic Response of Microbubbles Derived from Phase-Change Nanodroplet. *Jpn. J. Appl. Phys.* **2010**, *49* (7), 07HF18. https://doi.org/10.1143/JJAP.49.07HF18.
(26) Zhou, Y.; Wang, Z.; Chen, Y.; Shen, H.; Luo, Z.; Li, A.; Wang, Q.; Ran, H.; Li, P.; Song, W.; Yang, Z.; Chen, H.; Wang, Z.; Lu, G.; Zheng, Y. Microbubbles from Gas-Generating Perfluorohexane Nanoemulsions for Targeted Temperature-Sensitive Ultrasonography and Synergistic HIFU Ablation of Tumors. *Adv Mater* **2013**, *25* (30), 4123–4130. https://doi.org/10.1002/adma.201301655.
(27) Foroutan, F.; Jokerst, J. V.; Gambhir, S. S.; Vermesh, O.; Kim, H.-W.; Knowles, J. C. Sol–Gel Synthesis and Electrospraying of Biodegradable (P2O5) 55–(CaO) 30–(Na2O) 15 Glass Nanospheres as a Transient Contrast Agent for Ultrasound Stem Cell Imaging. *ACS nano* **2015**, *9* (2), 1868–1877.
(28) Chen, F.; Ma, M.; Wang, J.; Wang, F.; Chern, S.-X.; Zhao, E. R.; Jhunjhunwala, A.; Darmadi, S.; Chen, H.; Jokerst, J. V. Exosome-like Silica Nanoparticles: A Novel Ultrasound Contrast Agent for Stem Cell Imaging. *Nanoscale* **2017**, *9* (1), 402–411.
(29) Kwan, J. J.; Myers, R.; Coviello, C. M.; Graham, S. M.; Shah, A. R.; Stride, E.; Carlisle, R. C.; Coussios, C. C. Ultrasound-Propelled Nanocups for Drug Delivery. *Small* **2015**, *11* (39), 5305–5314. https://doi.org/10.1002/smll.201501322.
(30) Sazgarnia, A.; Shanei, A.; Taheri, A. R.; Meibodi, N. T.; Eshghi, H.; Attaran, N.; Shanei, M. M. Therapeutic Effects of Acoustic Cavitation in the Presence of Gold Nanoparticles on a Colon Tumor Model. *J Ultrasound Med* **2013**, *32* (3), 475–483. https://doi.org/10.7863/jum.2013.32.3.475.
(31) Guzmán, E.; Santini, E.; Ferrari, M.; Liggieri, L.; Ravera, F. Interfacial Properties of Mixed DPPC–Hydrophobic Fumed Silica Nanoparticle Layers. *J. Phys. Chem. C* **2015**, *119* (36), 21024–21034. https://doi.org/10.1021/acs.jpcc.5b07258.
(32) Mannelli, I.; Sagués, F.; Pruneri, V.; Reigada, R. Lipid Vesicle Interaction with Hydrophobic Surfaces: A Coarse-Grained Molecular Dynamics Study. *Langmuir* **2016**, *32* (48), 12632–12640. https://doi.org/10.1021/acs.langmuir.6b03364.
(33) Graupe, M.; Takenaga, M.; Koini, T.; Colorado, R.; Lee, T. R. Oriented Surface Dipoles Strongly Influence Interfacial Wettabilities. *Journal of the American Chemical Society* **1999**, *121* (13), 3222–3223.
(34) Sellers, H.; Ulman, A.; Shnidman, Y.; Eilers, J. E. Structure and Binding of Alkanethiolates on Gold and Silver Surfaces: Implications for Self-Assembled Monolayers. *J. Am. Chem. Soc.* **1993**, *115* (21), 9389–9401. https://doi.org/10.1021/ja00074a004.
(35) Yildirim, A.; Chattaraj, R.; Blum, N. T.; Goldscheitter, G. M.; Goodwin, A. P. Stable Encapsulation of Air in Mesoporous Silica Nanoparticles: Fluorocarbon-Free Nanoscale Ultrasound Contrast Agents. *Adv Healthc Mater* **2016**, *5* (11), 1290–1298. https://doi.org/10.1002/adhm.201600030.
(36) Parsons, J. E.; Cain, C. A.; Fowlkes, J. B. Spatial Variability in Acoustic Backscatter as an Indicator of Tissue Homogenate Production in Pulsed Cavitational Ultrasound Therapy. *IEEE Transactions on Ultrasonics, Ferroelectrics, and Frequency Control* **2007**, *54* (3), 576–590. https://doi.org/10.1109/TUFFC.2007.280.
(37) Rapoport, N.; Gao, Z.; Kennedy, A. Multifunctional Nanoparticles for Combining Ultrasonic Tumor Imaging and Targeted Chemotherapy. *JNCI: Journal of the National Cancer Institute* **2007**, *99* (14), 1095–1106. https://doi.org/10.1093/jnci/djm043.

(38) Levchenko, T. S.; Rammohan, R.; Lukyanov, A. N.; Whiteman, K. R.; Torchilin, V. P. Liposome Clearance in Mice: The Effect of a Separate and Combined Presence of Surface Charge and Polymer Coating. *International Journal of Pharmaceutics* **2002**, *240* (1–2), 95–102. https://doi.org/10.1016/S0378-5173(02)00129-1.
(39) Vu, T. Q.; Sant'Anna, L. E.; Kamat, N. P. Tuning Targeted Liposome Avidity to Cells via Lipid Phase Separation. *Biomacromolecules* **2023**, *24* (4), 1574–1584.
(40) Bompard, J.; Rosso, A.; Brizuela, L.; Mebarek, S.; Blum, L. J.; Trunfio-Sfarghiu, A.-M.; Lollo, G.; Granjon, T.; Girard-Egrot, A.; Maniti, O. Membrane Fluidity as a New Means to Selectively Target Cancer Cells with Fusogenic Lipid Carriers. *Langmuir* **2020**, *36* (19), 5134–5144.
(41) Izza, N.; Suga, K.; Okamoto, Y.; Watanabe, N.; Bui, T. T.; Wibisono, Y.; Fadila, C. R.; Umakoshi, H. Systematic Characterization of Nanostructured Lipid Carriers from Cetyl Palmitate/Caprylic Triglyceride/Tween 80 Mixtures in an Aqueous Environment. *Langmuir* **2021**, *37* (14), 4284–4293. https://doi.org/10.1021/acs.langmuir.1c00270.
(42) Li, L.; Zhan, Q.; Yi, K.; Chen, N.; Li, X.; Yang, S.; Hou, X.; Zhao, J.; Yuan, X.; Kang, C. Engineering Lipusu with Lysophosphatidylcholine for Improved Tumor Cellular Uptake and Anticancer Efficacy. *Journal of Materials Chemistry B* **2022**, *10* (11), 1833–1842. https://doi.org/10.1039/D1TB02823E.
(43) Zaidi, N.; Lupien, L.; Kuemmerle, N. B.; Kinlaw, W. B.; Swinnen, J. V.; Smans, K. Lipogenesis and Lipolysis: The Pathways Exploited by the Cancer Cells to Acquire Fatty Acids. *Progress in Lipid Research* **2013**, *52* (4), 585–589. https://doi.org/10.1016/j.plipres.2013.08.005.
(44) Mika, A.; Kobiela, J.; Pakiet, A.; Czumaj, A.; Sokołowska, E.; Makarewicz, W.; Chmielewski, M.; Stepnowski, P.; Marino-Gammazza, A.; Sledzinski, T. Preferential Uptake of Polyunsaturated Fatty Acids by Colorectal Cancer Cells. *Scientific Reports* **2020**, *10* (1), 1954.
(45) Abumanhal-Masarweh, H.; Da Silva, D.; Poley, M.; Zinger, A.; Goldman, E.; Krinsky, N.; Kleiner, R.; Shenbach, G.; Schroeder, J. E.; Shklover, J.; Shainsky-Roitman, J.; Schroeder, A. Tailoring the Lipid Composition of Nanoparticles Modulates Their Cellular Uptake and Affects the Viability of Triple Negative Breast Cancer Cells. *Journal of Controlled Release* **2019**, *307*, 331–341. https://doi.org/10.1016/j.jconrel.2019.06.025.
(46) Ashokkumar, M.; Lee, J.; Kentish, S.; Grieser, F. Bubbles in an Acoustic Field: An Overview. *Ultrasonics Sonochemistry* **2007**, *14* (4), 470–475. https://doi.org/10.1016/j.ultsonch.2006.09.016.
(47) Yildirim, A.; Chattaraj, R.; Blum, N. T.; Shi, D.; Kumar, K.; Goodwin, A. P. Phospholipid Capped Mesoporous Nanoparticles for Targeted High Intensity Focused Ultrasound Ablation. *Adv Healthc Mater* **2017**, *6* (18). https://doi.org/10.1002/adhm.201700514.
(48) Khattak, M. I. K.; Ahmed, N.; Umer, M. F.; Riaz, A.; Ahmad, N. M.; Khan, G. M. Chloroform-Injection (CI) and Spontaneous-Phase-Transition (SPT) Are Novel Methods, Simplifying the Fabrication of Liposomes with Versatile Solution to Cholesterol Content and Size Distribution. *Pharmaceutics* **2020**, *12* (11), 1065.
(49) Yildirim, A.; Shi, D.; Roy, S.; Blum, N. T.; Chattaraj, R.; Cha, J. N.; Goodwin, A. P. Nanoparticle-Mediated Acoustic Cavitation Enables High Intensity Focused Ultrasound Ablation Without Tissue Heating. *ACS Appl. Mater. Interfaces* **2018**, *10* (43), 36786–36795. https://doi.org/10.1021/acsami.8b15368.

(50) Yildirim, A.; Chattaraj, R.; Blum, N. T.; Goldscheitter, G. M.; Goodwin, A. P. Stable Encapsulation of Air in Mesoporous Silica Nanoparticles: Fluorocarbon-free Nanoscale Ultrasound Contrast Agents. *Advanced healthcare materials* **2016**, *5* (11), 1290–1298.
(51) Yildirim, A.; Chattaraj, R.; Blum, N. T.; Goodwin, A. P. Understanding Acoustic Cavitation Initiation by Porous Nanoparticles: Toward Nanoscale Agents for Ultrasound Imaging and Therapy. *Chem. Mater.* **2016**, *28* (16), 5962–5972. https://doi.org/10.1021/acs.chemmater.6b02634.
(52) Blum, N. T.; Yildirim, A.; Chattaraj, R.; Goodwin, A. P. Nanoparticles Formed by Acoustic Destruction of Microbubbles and Their Utilization for Imaging and Effects on Therapy by High Intensity Focused Ultrasound. *Theranostics* **2017**, *7* (3), 694.
(53) Chattaraj, R.; M. Goldscheitter, G.; Yildirim, A.; P. Goodwin, A. Phase Behavior of Mixed Lipid Monolayers on Perfluorocarbon Nanoemulsions and Its Effect on Acoustic Contrast. *RSC Advances* **2016**, *6* (112), 111318–111325. https://doi.org/10.1039/C6RA20328K.
(54) Chattaraj, R.; Mohan, P.; Besmer, J. D.; Goodwin, A. P. Selective Vaporization of Superheated Nanodroplets for Rapid, Sensitive, Acoustic Biosensing. *Advanced healthcare materials* **2015**, *4* (12), 1790–1795.
(55) Guzmán, E.; Martínez-Pedrero, F.; Calero, C.; Maestro, A.; Ortega, F.; Rubio, R. G. A Broad Perspective to Particle-Laden Fluid Interfaces Systems: From Chemically Homogeneous Particles to Active Colloids. *Advances in Colloid and Interface Science* **2022**, *302*, 102620. https://doi.org/10.1016/j.cis.2022.102620.
(56) Maestro, A.; Guzmán, E.; Ortega, F.; Rubio, R. G. Contact Angle of Micro- and Nanoparticles at Fluid Interfaces. *Current Opinion in Colloid & Interface Science* **2014**, *19* (4), 355–367. https://doi.org/10.1016/j.cocis.2014.04.008.
(57) Daecher, A.; Stanczak, M.; Liu, J.-B.; Zhang, J.; Du, S.; Forsberg, F.; Leeper, D. B.; Eisenbrey, J. R. Localized Microbubble Cavitation-Based Antivascular Therapy for Improving HCC Treatment Response to Radiotherapy. *Cancer Letters* **2017**, *411*, 100–105. https://doi.org/10.1016/j.canlet.2017.09.037.
(58) Rawicz, W.; Olbrich, K. C.; McIntosh, T.; Needham, D.; Evans, E. Effect of Chain Length and Unsaturation on Elasticity of Lipid Bilayers. *Biophysical Journal* **2000**, *79* (1), 328–339. https://doi.org/10.1016/S0006-3495(00)76295-3.
(59) Blum, N. T.; Yildirim, A.; Gyorkos, C.; Shi, D.; Cai, A.; Chattaraj, R.; Goodwin, A. P. Temperature-Responsive Hydrophobic Silica Nanoparticle Ultrasound Contrast Agents Directed by Phospholipid Phase Behavior. *ACS Appl. Mater. Interfaces* **2019**, *11* (17), 15233–15240. https://doi.org/10.1021/acsami.8b22659.
(60) Gu, Y.; Li, B.; Chen, M. An Experimental Study on the Cavitation of Water with Effects of SiO2 Nanoparticles. *Experimental Thermal and Fluid Science* **2016**, *79*, 195–201.
(61) Chen, Y.; Chang, J.; Bussonnière, A.; Xie, G.; Liu, Q. Evaluation of Wettability of Mineral Particles via Cavitation Thresholds. *Powder Technology* **2020**, *362*, 334–340. https://doi.org/10.1016/j.powtec.2019.11.069.
(62) Deng, C. X.; Xu, Q.; Apfel, R. E.; Holland, C. K. Inertial Cavitation Produced by Pulsed Ultrasound in Controlled Host Media. *The Journal of the Acoustical Society of America* **1996**, *100* (2), 1199–1208.
(63) Deng, C. X.; Xu, Q.; Apfel, R. E.; Holland, C. K. In Vitro Measurements of Inertial Cavitation Thresholds in Human Blood. *Ultrasound in medicine & biology* **1996**, *22* (7), 939–948.

(64) Roy, R. A.; Madanshetty, S. I.; Apfel, R. E. An Acoustic Backscattering Technique for the Detection of Transient Cavitation Produced by Microsecond Pulses of Ultrasound. *The Journal of the Acoustical Society of America* **1990**, *87* (6), 2451–2458.
(65) Chen, Y.; Chang, J.; Bussonnière, A.; Xie, G.; Liu, Q. Evaluation of Wettability of Mineral Particles via Cavitation Thresholds. *Powder Technology* **2020**, *362*, 334–340. https://doi.org/10.1016/j.powtec.2019.11.069.
(66) Subczynski, W. K.; Wisniewska, A.; Yin, J.-J.; Hyde, J. S.; Kusumi, A. Hydrophobic Barriers of Lipid Bilayer Membranes Formed by Reduction of Water Penetration by Alkyl Chain Unsaturation and Cholesterol. *Biochemistry* **1994**, *33* (24), 7670–7681. https://doi.org/10.1021/bi00190a022.
(67) Pinazo, A.; Wen, X.; Liao, Y.-C.; Prosser, A. J.; Franses, E. I. Comparison of DLPC and DPPC in Controlling the Dynamic Adsorption and Surface Tension of Their Aqueous Dispersions. *Langmuir* **2002**, *18* (23), 8888–8896. https://doi.org/10.1021/la020476r.
(68) Kučerka, N.; Nieh, M.-P.; Katsaras, J. Fluid Phase Lipid Areas and Bilayer Thicknesses of Commonly Used Phosphatidylcholines as a Function of Temperature. *Biochimica et Biophysica Acta (BBA) - Biomembranes* **2011**, *1808* (11), 2761–2771. https://doi.org/10.1016/j.bbamem.2011.07.022.
(69) Pinto, F.; Fonseca, L. P.; Souza, S.; Oliva, A.; de Barros, D. P. C. Topical Distribution and Efficiency of Nanostructured Lipid Carriers on a 3D Reconstructed Human Epidermis Model. *Journal of Drug Delivery Science and Technology* **2020**, *57*, 101616. https://doi.org/10.1016/j.jddst.2020.101616.
(70) Mueller, E. N.; Alina, T. B.; Curry, S. D.; Ganguly, S.; Cha, J. N.; Goodwin, A. P. Silica-Coated Gold Nanorods with Hydrophobic Modification Show Both Enhanced Two-Photon Fluorescence and Ultrasound Drug Release. *J. Mater. Chem. B* **2022**, *10* (47), 9789–9793. https://doi.org/10.1039/D2TB02197H.
(71) Rapoport, N.; Marin, A.; Luo, Y.; Prestwich, G. D.; Muniruzzaman, Md. Intracellular Uptake and Trafficking of Pluronic Micelles in Drug-Sensitive and MDR Cells: Effect on the Intracellular Drug Localization. *Journal of Pharmaceutical Sciences* **2002**, *91* (1), 157–170. https://doi.org/10.1002/jps.10006.
(72) Ho, J. C. S.; Ambite, I.; Mok, K. H.; Babjuk, M.; Svanborg, C. A Scientific Journey from Discovery to Validation of Efficacy in Cancer Patients: HAMLET and Alpha1-Oleate. *Mol Cell Oncol 8* (5), 1974278. https://doi.org/10.1080/23723556.2021.1974278.
(73) Bian, X.; Liu, R.; Meng, Y.; Xing, D.; Xu, D.; Lu, Z. Lipid Metabolism and Cancer. *J Exp Med* **2020**, *218* (1), e20201606. https://doi.org/10.1084/jem.20201606.
(74) Jülicher, F.; Lipowsky, R. Shape Transformations of Vesicles with Intramembrane Domains. *Phys. Rev. E* **1996**, *53* (3), 2670–2683. https://doi.org/10.1103/PhysRevE.53.2670.
(75) Dean, D. S.; Manghi, M. Fluctuation-Induced Interactions between Domains in Membranes. *Phys. Rev. E* **2006**, *74* (2), 021916. https://doi.org/10.1103/PhysRevE.74.021916.
(76) Suga, K.; Umakoshi, H. Detection of Nanosized Ordered Domains in DOPC/DPPC and DOPC/Ch Binary Lipid Mixture Systems of Large Unilamellar Vesicles Using a TEMPO Quenching Method. *Langmuir* **2013**, *29* (15), 4830–4838. https://doi.org/10.1021/la304768f.
(77) Carpenter, T. S.; López, C. A.; Neale, C.; Montour, C.; Ingólfsson, H. I.; Di Natale, F.; Lightstone, F. C.; Gnanakaran, S. Capturing Phase Behavior of Ternary Lipid Mixtures with a Refined Martini Coarse-Grained Force Field. *J. Chem. Theory Comput.* **2018**, *14* (11), 6050–6062. https://doi.org/10.1021/acs.jctc.8b00496.

(78) Zhao, J.; Wu, J.; Heberle, F. A.; Mills, T. T.; Klawitter, P.; Huang, G.; Costanza, G.; Feigenson, G. W. Phase Studies of Model Biomembranes: Complex Behavior of DSPC/DOPC/Cholesterol. *Biochim Biophys Acta* **2007**, *1768* (11), 2764–2776. https://doi.org/10.1016/j.bbamem.2007.07.008.
(79) Veatch, S. L.; Keller, S. L. Organization in Lipid Membranes Containing Cholesterol. *Phys. Rev. Lett.* **2002**, *89* (26), 268101. https://doi.org/10.1103/PhysRevLett.89.268101.